Outstanding cracking resistance in Mg-alloyed zinc coatings achieved via crystallographic texture control

Ahmadi, Masoud; Salgın, Bekir; Kooi, Bart J.; Pei, Yutao

Published in:
Scripta Materialia

DOI:
10.1016/j.scriptamat.2021.114453

Publication date:
2022

Scripta Materialia 210 (2022) 114453

Contents lists available at ScienceDirect

Scripta Materialia

journal homepage: www.elsevier.com/locate/scriptamat

Outstanding cracking resistance in Mg-alloyed zinc coatings achieved via crystallographic texture control

Masoud Ahmadi[a], Bekir Salgın[b], Bart J. Kooi[c], Yutao Pei[a,*]

[a] Department of Advanced Production Engineering, Engineering and Technology Institute Groningen, Faculty of Science and Engineering, University of Groningen, Nijenborgh 4, 9747AG Groningen, the Netherlands
[b] Tata Steel, Research & Development, P.O. Box 10000, 1970CA IJmuiden, the Netherlands
[c] Nanostructured Materials and Interfaces, Zernike Institute for Advanced Materials, Faculty of Science and Engineering, University of Groningen, Nijenborgh 4, 9747AG Groningen, the Netherlands

ARTICLE INFO

Article history:
Received 23 August 2021
Revised 12 November 2021
Accepted 27 November 2021

Keywords:
Cracking resistance
Zn-Al-Mg coatings
Crystallographic texture
Formability

ABSTRACT

Cracking limits the formability of Mg-alloyed zinc coatings on steel substrates. Unfavorable crystal orientations and brittle microstructural components serve as the main sources of cracks in these coatings. In this study, we overcome the deformation-induced cracking and substantially enhance the formability of Zn-Al-Mg coatings by controlling their crystallographic texture. To demonstrate this, in-situ scanning electron microscopy uniaxial tensile tests and thorough orientation image microscopy have been employed. Ultimately, we validate our findings by implementing quantitative plastic deformation-based criteria, namely local strain hardening exponent and Schmid factor distributions within the examined coating microstructures. The approach and findings of the present work considerably resolve the long-lasting cracking problem of these coatings.

Zinc alloys are important coating materials that have been widely used due to their corrosion resistance, biocompatibility and natural abundance [1,2]. Amongst zinc-based coatings, Zn-Al-Mg coatings have attracted a lot of attention owing to their excellent corrosion resistance. Nevertheless, Mg-alloyed zinc coatings possess poor cracking resistance and formability in general [3,4]. Suppressing the undesirable initiation and propagation of the cracks has persisted as a significant challenge. It is therefore crucial to apply effective solutions in order to attain a crack-free and highly formable Mg-alloyed zinc-based coating.

Mechanical behaviors of pure zinc and zinc alloy coatings have been evaluated with regard to orientation, microstructure, damage, adhesion and formability [5–14]. On the other hand, deformation-induced cracking in zinc alloy coatings has been an enduring concern for decades. In contrast to the hot-dip galvanized pure zinc coatings that mostly exhibit intergranular cracking, Zn-Al-Mg coatings suffer from severe transgranular cracking under deformation. The microstructure of these coatings is typically composed of primary zinc grain (Zn), coarse binary eutectic (BE) and fine ternary eutectic (TE) [15]. The core source of micro-cracking in these coatings has been attributed to the brittle and coarse BE component of the coating's microstructure as revealed in our previous study [15,16]. Moreover, unfavorable crystallographic orientations of the grains can significantly lead to in-grain cracks and crack propagation within the microstructure [15,17]. For Mg-alloyed zinc coatings, there is still a lack of systematic work on fostering a desirable texture that can enhance the cracking resistance and formability.

As a key step towards achieving highly formable Mg-alloyed zinc coatings, this study provides remarkable enhancement of the cracking resistance by tailoring the crystallographic texture. In the present study, we firstly elucidate the considerable improvement of the cracking resistance by tailoring the crystallographic texture in the BE-containing ZnAlMg coatings. Secondly, for the first time we unfold the advantage of simultaneous microstructure and texture control by a BE-free coating that ultimately results in superb crack-resistance and formability properties. To confirm our findings, we have incorporated quantitative plastic deformation-based criteria including local orientation-dependent strain hardening exponent and Schmid factor distributions.

In this study, four ZnAlMg coatings on steel substrates produced by an annealing hot-dip simulator are investigated. The specimens are labelled as follows. Coating C1: a BE-containing ZnAlMg coating with 1.7–2.0 wt.% Al and 1.7–2.0 wt.% Mg on a steel substrate type 1; Coating C2: a BE-containing ZnAlMg coating with 1.7–2.0 wt.% Al and 1.7–2.0 wt.% Mg on a steel substrate type

* Corresponding author at: Advanced Production Engineering, Engineer and Technology Institute Groningen, University of Groningen, Nijenborgh 4, 9747AG Groningen, the Netherlands.
E-mail address: y.pei@rug.nl (Y. Pei).

https://doi.org/10.1016/j.scriptamat.2021.114453

2; Coating C3: a texture controlled BE-containing ZnAlMg coating with 1.7–2.0 wt.% Al and 1.7–2.0 wt.% Mg on a steel substrate type 2; Coating C4: a simultaneously texture and microstructure controlled BE-free ZnAlMg coating with 2.9 wt.% Al and 1.9 wt.% Mg on a steel substrate type 2. The fraction of BE in the BE-containing coatings (i.e. C1, C2, C3) is found to be 16.5% on average, whereas the BE-free coating C4 has a residual BE of less than 0.7%. The texture control has been performed by tuning the galvanizing process parameters.

Tensile specimens were cut from the hot-dip galvanized sheets and subjected to mechanical polishing utilizing 1 μm diamond suspension. The samples were then ion polished employing a JEOL IB-19520CCP ion polisher. Prior to electron backscatter diffraction (EBSD) analysis, the in-situ tensile tests were conducted up to 0.1 true strain by means of a Kammrath & Weiss tensile module in a scanning electron microscope (Tescan LYRA SEM–FIB).

In order to capture the crystallographic textures of the coatings, orientation image microscopy (OIM) analysis was carried out using an EBSD-equipped Philips XL30 ESEM. For an efficient EBSD measurement, 500 nm scanning step size and 30 kV accelerating voltage were employed. The EBSD analyses were executed on the specimens' surface at the center of their gauge length. Texture calculations and crystallographic orientation dependent information were identified by performing EBSD analysis using EDAX-TSL OIM™ Analysis 8 package. Schmid factor distributions were calculated by applying the primary slip systems of HCP Zn [15].

To validate the EBSD texture measurements and assess the orientation distributions in a statistical manner, a large area (9 cm^2) of the coatings was exposed to XRD texture evaluations. These measurements were recorded using a Bruker D8 Discover diffractometer equipped with an area-sensitive detector (Vantec 500).

The orientation-dependent local strain hardening exponent (n) values were calculated based on a methodology introduced in our previous study [15]. The following empirical equation for Mg-alloyed zinc coatings was applied:

$$n = 1.428 \times 10^{-8}\theta^4 - 2.233 \times 10^{-6}\theta^3 + 1.027 \times 10^{-4}\theta^2 - 4.631 \times 10^{-4}\theta + 0.29 \quad (1)$$

where θ is the orientation angle of the grains, namely the angle between the c-axis of HCP Zn grains and the applied loading direction. This equation relates crystallographic orientations to the formability properties and cracking tendency of the Zn grains.

Fig. 1 displays the results of the EBSD analysis on the coating C1 after in-situ tensile testing up to 0.1 true strain. Image quality (IQ) merged with the inverse pole figure (IPF) map is depicted in Fig. 1a. The harmonic textures by pole figure (PF) are demonstrated in Fig. 1b. Fig. 1c presents the IQ map including labelled grains showing cracks in the deformed microstructure. Fig. 1d provides the orientation-dependent local strain hardening exponent (n) and Schmid factor (m) distributions associated with coating C1. As it can be observed in Fig. 1, coating C1 exhibits quite weak crystallographic texture. Some primary zinc grains and eutectic regions experience cracking during the deformation. Orientation-related information of the large cracks formed after deformation, as labelled in Fig. 1c, is given in Table 1.

As Table 1 indicates, the grains with low n-values (i.e. $n < 0.33$) and low m-values (i.e. $m < 0.32$) underwent cracking. The majority of the cracks originated in the brittle BE component and propagated through the adjacent Zn grains with low m and n values. These observations are in good agreement with our previous study on the cracking behavior of the ZnAlMg coatings. In particular, it has been shown that the unfavorably oriented Zn grains with low n-values ($n < 0.33$) and low m-values ($m < 0.32$) lack the required deformation mechanisms through dislocation slip and are therefore highly prone to cracking during straining [15]. In contrast, the favorably oriented grains (e.g. G18) well aligned with (0001) pole parallel to the surface normal, possess large n and m values and thus resist cracking. Here, 30% of the C1 microstructure exhibit $n < 0.33$ and 12% are of $m < 0.32$ (see Fig. 1d) within the studied area. This consequently boosts the probability of transgranular crack propagation within the C1 microstructure. Therefore, both BE and unfavorably oriented Zn grains contribute to the cracking observed in the coating. BE regions are the primary sites for crack initiation, and the adjacent Zn grains with unfavorable orientations (i.e. exhibiting low n and m values) propagate the initiated cracks through. The detailed description of the mechanism of cracking in Zn-Al-Mg coatings can be found in our previous study [15].

Table 1
Crystallographic orientation related information, in particular local strain hardening exponent (n) and Schmid factor (m) values, of the grains labelled in Fig. 1c.

Grain No.	n-value	m-value	cracked
G1	0.289	0.11	Yes
G2	0.296	0.23	Yes
G3	0.289	0.11	Yes
G4	0.308	0.29	Yes
G5	0.292	0.15	Yes
G6	0.308	0.3	Yes
G7	0.299	0.27	Yes
G8	0.293	0.16	Yes
G9	0.293	0.16	Yes
G10	0.297	0.24	Yes
G11	0.295	0.21	Yes
G12	0.289	0.12	Yes
G13	0.293	0.15	Yes
G14	0.295	0.19	Yes
G15	0.295	0.2	Yes
G16	0.292	0.15	Yes
G17	0.289	0.09	Yes
G18	0.348	0.47	No

Fig. 2 illustrates the EBSD results of the coating C2 subjected to uniaxial tensile test up to 0.1 true strain. As it can be conceived, this coating also exhibits a quite dispersed texture distribution. The coating shows a large number of cracks after the imposed deformation (see Fig. 2c). Within the examined area, 25% of the microstructure possess low strain hardening exponent (i.e. $n < 0.33$) as Fig. 2d indicates. Hence, a high fraction of grains is present with a low capacity to plastically deform, which serve as crack propagating sites during the deformation.

The results of the EBSD analyses on the texture-controlled C3 coating and the texture + microstructure controlled C4 coating after uniaxial tension are given in Fig. 3 and Fig. 4, respectively. The complete characteristics of all the examined coatings and the cracking quantification results are given and compared in Table 2. The results of the XRD texture measurements prior to the deformations are provided in Fig. S1 of the supplementary material for the sake of statistical validation of the EBSD analyses. The cracking quantifications are executed using image analysis based on the SEM micrographs of higher magnifications captured from the studied areas of the coatings such as presented in Fig. 5.

As it can be noticed in Fig. 3b, a relatively concentrated (0001) fiber texture is obtained in the binary eutectic containing C3. This is confirmed by the IPF map in Fig. 3a, unveiling that the majority of the grains shows up in red. The fraction of the harmful orientation incidents (i.e. grains with $n < 0.33$) are notably reduced in C3 as shown in Fig. 3d. Yet, a fully concentrated and strong (0001) fiber texture is achieved for the C4 case as Fig. 4b displays. The maximum texture intensity is substantially increased from 3.5 for C1 to 24.5 for C4 as listed in Table 2. The C4 microstructure exhibits zinc grains dominant with favorable (0001) orientation that delivers pretty high n and m values (as the formability criteria) shown in Fig. 4d. To compare the cracking tendency among the deformed coatings, one can notice that C4 and C3 offer considerable

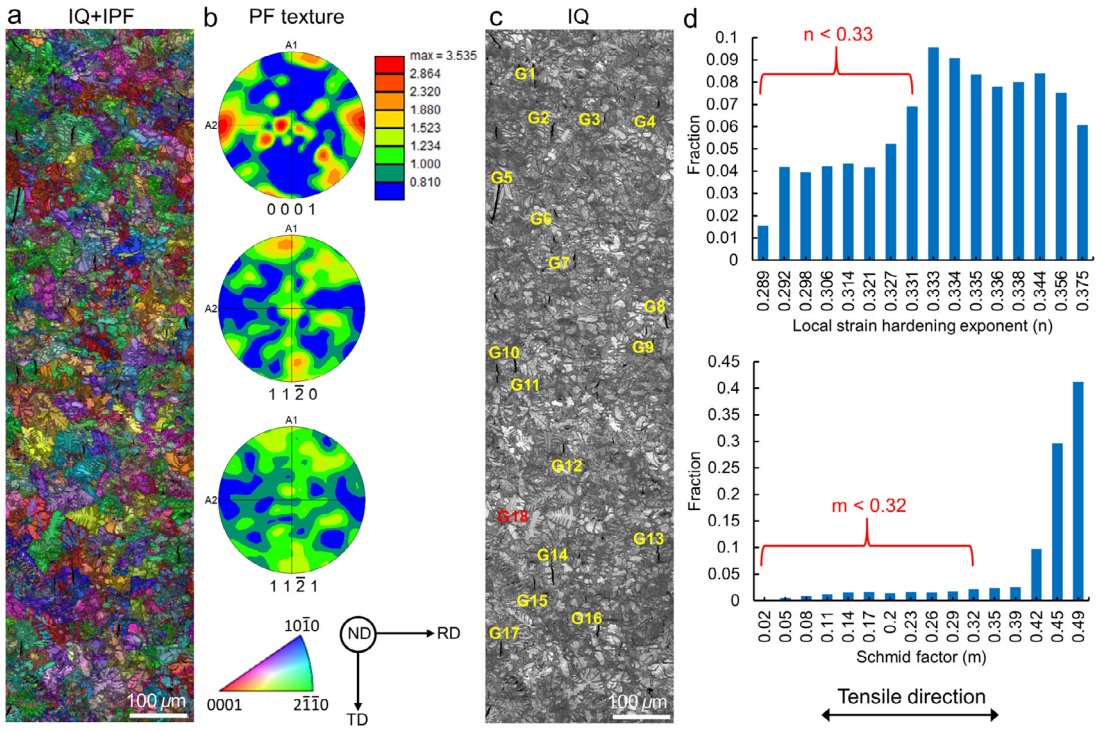

Fig. 1. EBSD results of the coating C1 subjected to in-situ tensile test up to 0.1 true strain, (a) IQ plus IPF map, (b) harmonic texture representation by PFs, (c) IQ map and the labelled grains, (d) distributions of local strain hardening exponent (n) and Schmid factor (m) values within the examined microstructure.

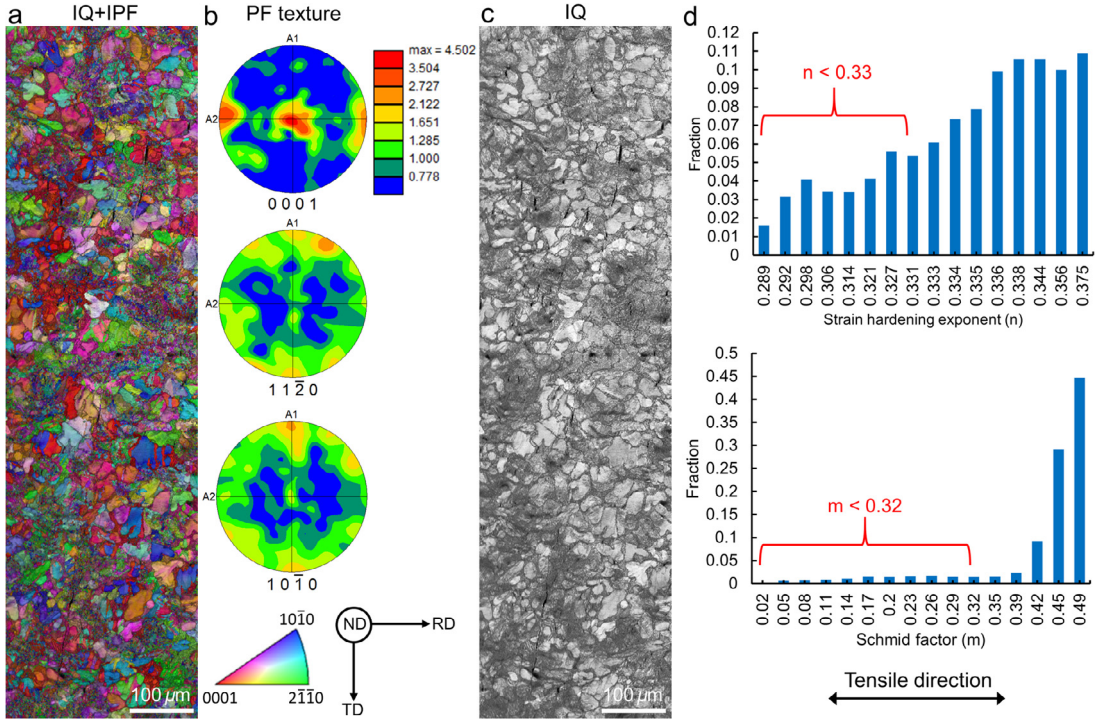

Fig. 2. EBSD results of the coating C2 subjected to in-situ tensile test up to 0.1 true strain, (a) IQ plus IPF map, (b) harmonic texture representation by PFs, (c) IQ map showing cracks, (d) distributions of n and m values within the examined microstructure.

Table 2
The information and cracking quantification results of all the examined coatings.

Coating label	Microstructure	Steel substrate	Texture type	Max. texture intensity	Total No. of cracks	No. of cracked Zn grains	Average crack length (μm)
C1	Zn + BE + TE	type 1	dispersed	3.5	92	18	21.4
C2	Zn + BE + TE	type 2	dispersed	4.5	83	14	20.3
C3	Zn + BE + TE	type 2	nearly concentrated	10	26	2	6.4
C4	Zn + TE	type 2	fully concentrated	24.5	5	0	3.6

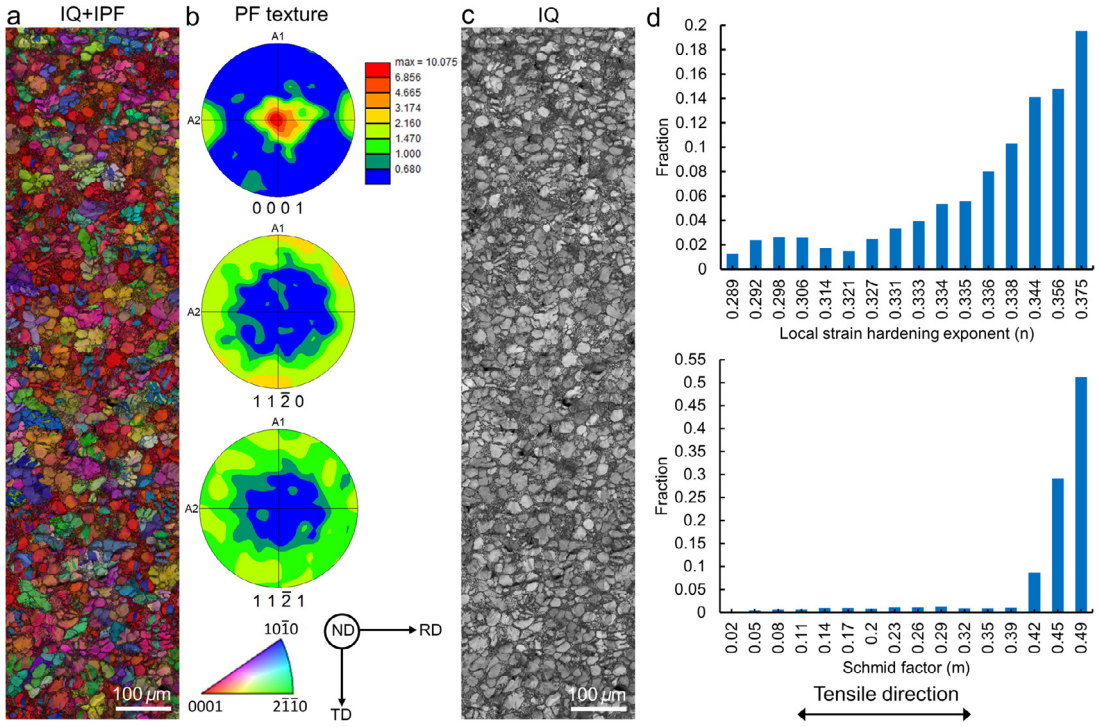

Fig. 3. EBSD results of the coating C3 subjected to in-situ tensile test up to 0.1 true strain, (a) IQ plus IPF map, (b) harmonic texture representation by PFs, (c) IQ map revealing substantial cracking resistance (d) distributions of n and m values within the examined microstructure.

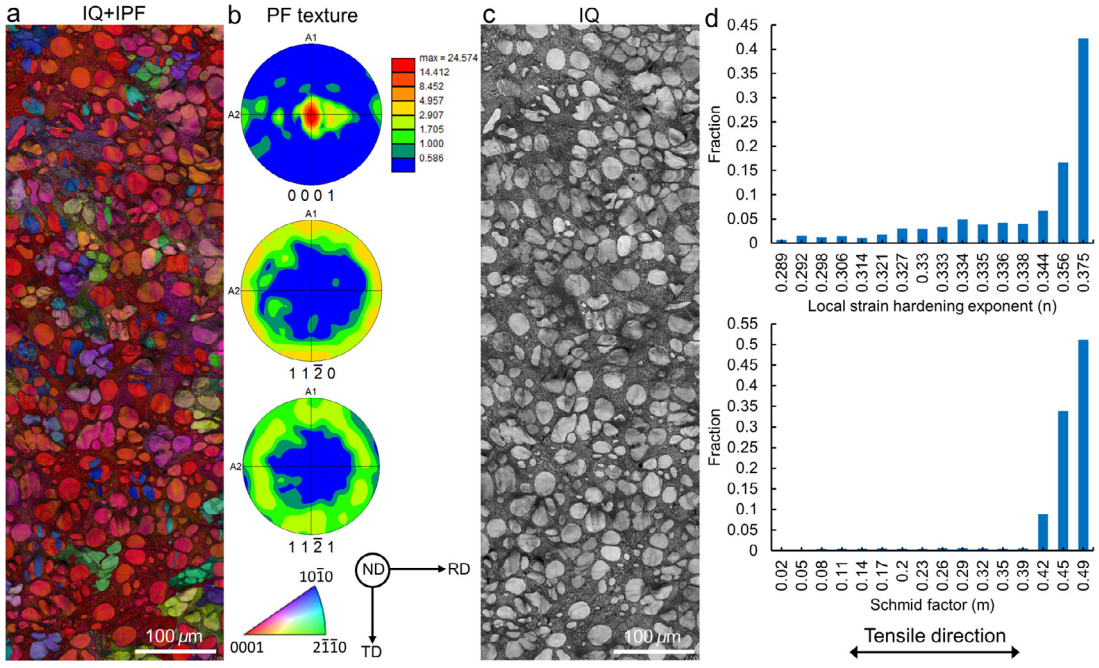

Fig. 4. EBSD results of the coating C4 subjected to in-situ tensile test up to 0.1 true strain, (a) IQ plus IPF map, (b) harmonic texture representation by PFs, (c) IQ map revealing outstanding cracking resistance, (d) distributions of n and m values within the examined microstructure.

reduction in the number density and average length of the cracks in comparison with C1 and C2. The total number of the cracks (per studied areas) are counted as 92 and 83 for the C1 and C2, whereas they are reduced to 26 and 5 for C3 and C4, respectively. C1 and C2 coated on different steel substrates both exhibit very poor cracking resistance due to their random and dispersed texture. The cracking resistance and formability are considerably enhanced in C3 possessing a nearly concentrated (0001) texture. Although C3 entails the main source of micro-cracks within binary eutectics, it shows quite improved resistance against crack propagation compared to other BE-containing coatings (i.e. C1 and C2) owing to its favorable texture. In other words, while the tiny micro-cracks may nucleate in the binary eutectics (see Fig. 5(c)), the favorable orientation of the primary zinc grains in C3 restrains further transgranular crack propagations. This is confirmed by the low number of cracked primary Zn grains (i.e. 2) detected within the observation area of C3. Via the unique combination of crystallographic texture control and tailoring the coating microstructure (i.e. elimination of

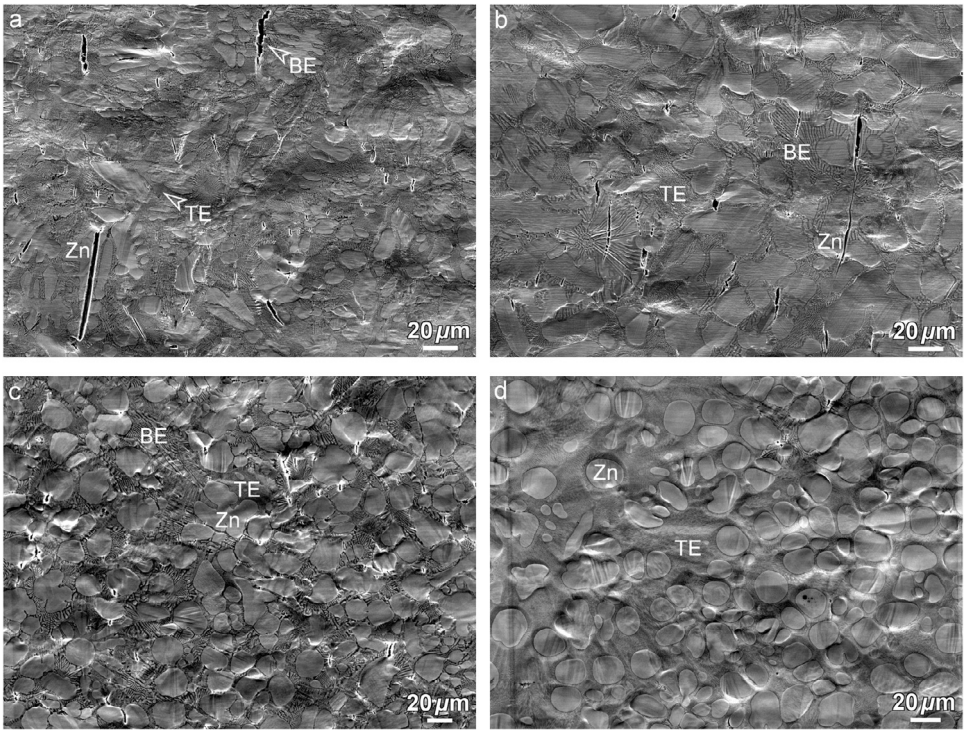

Fig. 5. Representative SEM micrographs of the studied areas showing the cracking tendencies of the coatings: (a) C1, (b) C2, (c) C3 and (d) C4 deformed to true strain of 0.1.

the BE) in C4, superb cracking resistance and formability are ultimately achieved as confirmed by the results given in Fig. 4 and Table 2. It should be noticed that no primary zinc grain has experienced cracking during the deformation of C4. The average length of the cracks has dropped substantially from 21.4 and 20.3 μm for C1 and C2 to 3.6 μm for C4. These scarce micro-cracks (< 4 μm) in C4 are merely formed in the minute amount of retained binary eutectic (as depicted in Fig. 5(d)) and confined between the well-orientated primary zinc grains (possessing high n and m values). These micro-cracks are therefore unable to propagate to form a long crack with large opening. The substantial enhancements of the cracking resistance attained in the texture-controlled C3 and C4 considerably outperform the cracking tendency of C2 coated on the same steel substrate type.

Zinc and its alloys possess HCP lattice structure with a $c/a = 1.856$ (higher than an ideal $c/a = 1.632$) that gives rise to the development of anisotropic properties under various loading conditions [18]. The inherent crystal anisotropy and complex microstructural features determine the deformation behavior and the formability of zinc-based coatings. In principle, the crystallographic orientation-related phenomena including cleavage, micro-cracking and deformation mechanisms strongly depend on the collective texture of a zinc alloy coating. Amongst the slip systems of Zn crystals, basal and pyramidal $<c + a>$ slip systems are found more likely to be activated during uniaxial tension [18]. In order to increase the probability of activation of primary slip systems in HCP Zn grains, (0001) texture control is employed and validated by quantitative criteria in the present study. In particular, basal slip is identified as the most easily activated dislocation slip system with the lowest required critical resolved shear stress [19]. Nevertheless, the typical Mg-alloyed zinc coating exhibits a dispersed texture that can hinder activation of such basal slips (see Figs. 1-2) and subsequently facilitates cracking. In other words, by the presence of some unfavorable crystal orientations (especially those crystals whose c-axes are parallel to the loading direction) within the microstructure, the possibility of transgranular crack propagation increases (see Fig. 5a-b). Thus, in the cases of C1 and C2, these unfavorable orientations are abundant and lead to severe micro-cracking. On the other hand, C3 and C4 coatings deliver a concentrated (0001) fiber texture that enhance the activation of basal slip with respect to the applied tensile force. In C3 and C4, the grains exhibit homogenous crystallographic orientation distribution aligned in order to prevent crack propagation. Therefore, instead of undergoing cracking (e.g. cleavage) [20], the microstructure of C3 and C4 can effectively accommodate plastically the imposed deformation. Furthermore, by obtaining a uniform and concentrated (0001) texture, the possibility of slip transmission across the grains/phases enhances drastically [21]. Since the misorientation among the grains decreases by a uniform texture, it is expected that C3 and C4 can facilitate plastic deformation through easy slip transmission. In the optimum case, the BE-free coating C4 does not entail the *crack nucleation* sites (i.e. coarse binary eutectics) on one hand and further exhibits a highly concentrated (0001) fiber texture to suppress *crack propagation* on the other hand, which offers outstanding crack-resistance, ductility and formability. It is worth mentioning that the other properties of these coatings (e.g. corrosion resistance) can be influenced by the texture control. For instance, it is reported [22] that the corrosion resistance of zinc-based coatings can be enhanced by increasing the (0001) basal component. Therefore, one expects that the corrosion behavior of the texture-controlled coatings in this work might be also improved as a result, yet this aspect should be separately studied in detail.

In summary, the cracking resistance of Mg-alloyed zinc coatings is substantially enhanced by applying crystallographic texture control. It is demonstrated here that in ZnAlMg coatings with tailored sharp (0001) fiber texture, transgranular crack propagation through primary zinc grains is almost completely prevented. Moreover, simultaneous texture and microstructure control ultimately offers a nearly crack-free ZnAlMg coating during tensile deformation, be-

cause the absence of binary eutectic prevents crack nucleation and the (0001) fiber texture suppresses crack propagation. The present work opens a gateway towards next-generation highly formable Zn-Al-Mg coatings.

Declaration of Competing Interest

The authors declare that they have no known competing financial interests or personal relationships that could have appeared to influence the work reported in this paper.

Funding

This research was funded under project number S22.3.15576/15440 by the Partnership Program of the Materials innovation institute M2i (www.m2i.nl) and the Technology Foundation TTW (www.stw.nl), which is part of the Netherlands Organization for Scientific Research (www.nwo.nl).

Supplementary materials

Supplementary material associated with this article can be found, in the online version, at doi:10.1016/j.scriptamat.2021.114453.

References

[1] S. Zhu, C. Wu, G. Li, Y. Zheng, J.-F. Nie, Mater. Res. Lett. 7 (2019) 347–353.
[2] B.W. Çetinkaya, F. Junge, G. Müller, F. Haakmann, K. Schierbaum, M. Giza, J. Mater. Res. Technol. 9 (2020) 16445–16458.
[3] E. De Bruycker, Z. Zermout, B.C. De Cooman, Mater. Sci. Forum. 539-543 (2007) 1276–1281.
[4] R. Parisot, S. Forest, A. Pineau, F. Grillon, X. Demonet, J.M. Mataigne, Metall. Mater. Trans. A Phys. Metall. Mater. Sci. 35 A (2004) 797–811.
[5] J.T.M. De Hosson, N. van der Pers, W.G. Sloof, G.M. Song, T. Vystavel, Acta Mater 60 (2012) 2973–2981.
[6] J. Legendre, R. Créac'Hcadec, A. Tanguy, S. Hallais, J.-.H. Schmitt, E. Héripré, F. Gilbert, D. Jacquet, J.M. Mataigne, Mater. Sci. Eng. A. 763 (2019) 138156.
[7] G.-.M. Song, W.G. Sloof, Mater. Sci. Eng. A. 528 (2011) 6432–6437.
[8] M. Safaeirad, M.R. Toroghinejad, F. Ashrafizadeh, J. Mater, Process. Technol. 196 (2008) 205–212.
[9] G. Li, X. Long, Coatings 10 (2020) 202.
[10] B. Hutchinson, J. Komenda, S. Kada, M. Barnett, A. Oskarsson, Scr. Mater. 166 (2019) 78–80.
[11] A. Chakraborty, D. Bhattacharjee, R. Pais, R.K. Ray, Scr. Mater. 57 (2007) 715–718.
[12] F. Zhang, G. Vincent, Y.H. Sha, L. Zuo, J.J. Fundenberger, C. Esling, Scr. Mater. 50 (2004) 1011–1015.
[13] G. Vincent, F. Zhang, J.J. Fundenberger, C. Esling, Scr. Mater. 53 (2005) 775–779.
[14] D. Bhattacharya, L. Cho, E. van der Aa, H. Ghassemi-Armaki, A. Pichler, K.O. Findley, J.G. Speer, Scr. Mater. 175 (2020) 49–54.
[15] M. Ahmadi, B. Salgın, B.J. Kooi, Y. Pei, Mater. Des. 186 (2020) 108364.
[16] M. Ahmadi, B. Salgın, M. Ahmadi, B.J. Kooi, Y. Pei, Int. J. Plast. (2021) 103041.
[17] Y.B. Park, I.G. Kim, S.G. Kim, W.T. Kim, T.C. Kim, M.S. Oh, J.S. Kim, Metall. Mater. Trans. A Phys. Metall. Mater. Sci. 48 (2017) 1013–1020.
[18] L. Cauvin, B. Raghavan, S. Bouvier, X. Wang, F. Meraghni, Mater. Sci. Eng. A. 729 (2018) 106–118.
[19] Y.T. Pei, G.M. Song, W.G. Sloof, J.T.M. De Hosson, Surf. Coatings Technol. 201 (2007) 6911–6916.
[20] G.M. Hughes, G.E. Smith, P.E.J. Flewitt, A.G. Crocker, Proc. R. Soc. A Math. Phys. Eng. Sci. 463 (2007) 2129–2151.
[21] T.R. Bieler, P. Eisenlohr, C. Zhang, H.J. Phukan, M.A. Crimp, Curr. Opin. Solid State Mater. Sci. 18 (2014) 212–226.
[22] H. Asgari, M.R. Toroghinejad, M.A. Golozar, J. Mater. Process. Technol. 198 (2008) 54–59.